Final project

Certificate of geomatics

Evolution of the Snow Water Equivalent during 2018 over Bretaye basin

Lac de Bretaye, Ollon. ©Roland Kunz. Accessible via https://notrehistoire.ch/entries/lyYnlMLb8E9

20th August 2025
Julien Kessler

UNIVERSITÉ DE GENÈVE

UNIVERSITÉ DE GENÈVE

Table of Contents

Introduction

Groundwater plays a critical role in determining lake chemistry, particularly in lakes primarily fed by precipitation (Gurrieri et Furniss 2004). As precipitation typically exhibits low electrical conductivity and is deficient in nutrients, groundwater—rich in dissolved elements—becomes a key regulator of chemical inputs. Even when groundwater constitutes a minor component of the annual hydrological budget, it can serve as a significant source of nutrients for phytoplankton, especially in lakes influenced by snowmelt (Hurley et al. 1985). This is the case for the three alpine lakes within the studied watershed.

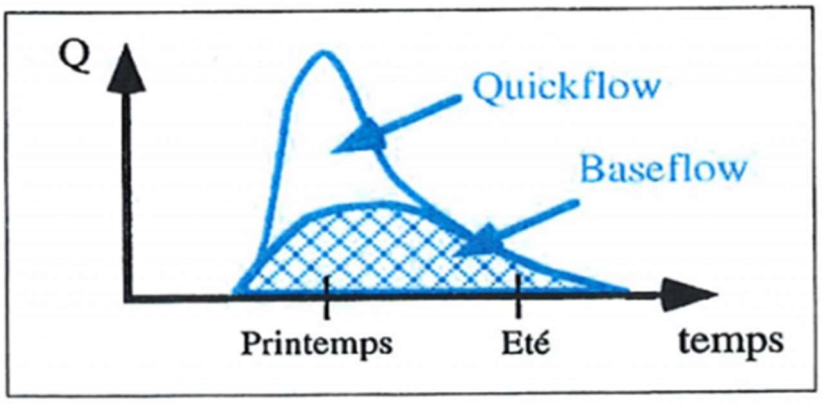

Figure 1: Baseflow vs Quickflow (Parriaux, 1997)

In these alpine systems, a period of heightened biological activity occurs during summer, when both precipitation and snowmelt are reduced. During this time, groundwater exhibits higher conductivity due to limited dilution from meteoric inputs (Parriaux 1997). For instance, a study conducted on an oligotrophic lake in Wisconsin revealed that although groundwater accounted for less than 10% of the lake's annual water volume, it delivered nearly the entire external silica load—an essential nutrient for diatom growth (Hurley et al. 1985). Diatom blooms in that system were found to coincide with peak silica concentrations supplied by groundwater.

These lakes typically follow a "quickflow–baseflow" hydrological regime: quickflow refers to periods of high discharge driven by autumn rainfall and spring snowmelt, whereas baseflow characterizes more hydrologically stable periods with reduced water inputs, typical of summer and early winter (Parriaux 1997) (Fig.1). Parriaux et al. (1997) measured the electrical conductivity of the Poutet spring—located beneath the Chamossaire watershed—over the course of a year and observed substantial variability (*Cmax/Cmin* = 2.73). This variation is attributed to low conductivity during quickflow events, resulting from the substantial dilution of Poutet spring waters by snowmelt and autumn rainfall. These episodes are characterized by a rapid influx of weakly mineralized water, reducing the conductivity to a minimum of 240 µS cm^{-1}. Following these events, conductivity gradually returns to its baseline value, reaching approximately 650 µS cm^{-1} during baseflow periods (Parriaux 1997).

Complementarily, a conductivity profiles through the water column of Lake Bretaye has been done in 2018 (Ordóñez 2022), revealing notable vertical variability. Two distinct conductivity peaks were recorded near the lake bottom: 268 µS cm^{-1} on June 16, 2018, and 548 µS cm^{-1} on September 2, 2018. Based on the findings of Parriaux (1997), the abrupt influx of poorly mineralized meltwater leads to a transient decrease in overall mineral content, suggesting that these conductivity peaks are likely associated with groundwater inputs.

Problem statement and research objectives

Figure 2 presents the water level of Lake Bretaye, based on data from the study conducted by Ordóñez (2022). The figure appears to depict the end of the 2018 quickflow period, characterized by a decline in lake level between June 21 and July 15, followed by a phase with a more stable, linear rate of decrease. This interpretation is consistent with the conductivity measurements reported by both Ordóñez (2022) and Parriaux (1997), supporting the transition from a period of high inflow dominated by dilute snowmelt to a more stable baseflow regime.

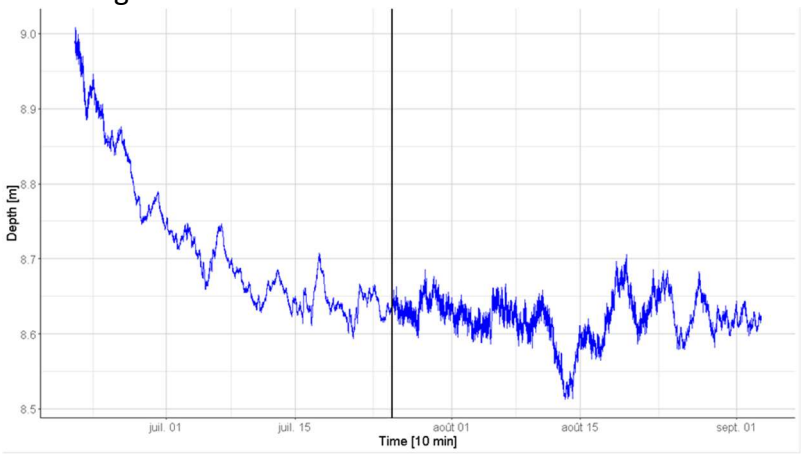

Figure 2: Lake Bretaye water level; the black line indicates the point at which the research team retrieved the data before redeploying the sensors.

To better understand the seasonal dynamics of the three lakes—whose seasonality plays a critical role in shaping their biodiversity—this study focuses on the evolution of snowmelt during the year 2018. This reference year allows for direct comparison with the results reported by Ordòñez (2022). The objective is to improve our understanding of the hydrogeological processes governing these environments by examining the temporal evolution of the winter quickflow period, characterized by snowmelt-driven inflows.
A master thesis has been done on this watershed, with the purpose to estimate the groundwater activity ok the lake, based on Ordòñez (2022) datasets. This study shows that a possible missing flow, due to snowpack, is probably occurring during the month of June. Figure 3 below shows the monthly result of this study. $Q_{out,WMB}$ is the residual flow, which is the difference between the mean lake level variability and the sum of evaporation and precipitation. This residual flux is likely to be driven by groundwater activity and snowpack, the two major unknown.

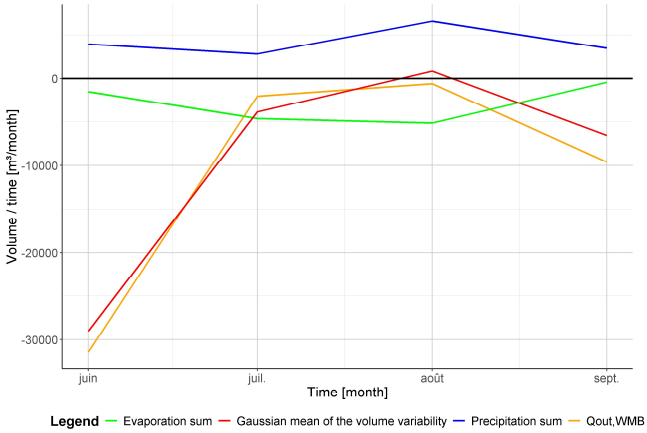

Figure 3: Mean Lake volume variability, evaporation sum, and precipitation sum and residual flux on a monthly time base

State of art

Snow Water Equivalent

To quantify the total Snow Water Equivalent (*SWE*) over a watershed, the basin must first be delineated using a Digital Elevation Model (*DEM*) and exported as a shapefile. The *SWE* values are then spatially integrated over the watershed to compute the total snow water volume.

Ideally, these remote sensing estimates should be validated against ground-based observations. However, in the absence of such data, model-based approaches must be relied upon.

The spatial extent of snow cover is generally assessed using optical sensors such as MODIS or Sentinel-2. In this context, the Normalized Difference Snow Index (*NDSI*) is frequently employed to distinguish snow-covered areas from other land surfaces (Equ. 1) (Dozier 1989).

$$NDSI = (\rho_{Green} - \rho_{SWIR}) / (\rho_{Green} + \rho_{SWIR}) \quad (1)$$

Traditional approaches to estimating *SWE* rely on the product of snow depth and snow density, often derived from a combination of radar, lidar, and in-situ measurements (Rabatel et al., 2017; Niang et al., 2006). However, these methods are limited by the availability of high-resolution data and the difficulty of accurately modeling snow density across heterogeneous terrain. The estimation of snow water equivalent is commonly expressed as the product of the mean snow density and the snow depth (Equ. 2) (Rabatel et al. 2017), where *SWE* is the snow water equivalent, h_{snow} is the snow depth, ρ_{snow} is the mean snow density.

$$SWE = h_{snow} \times \rho_{snow} \quad (2)$$

Snow depth can be estimated using remote sensing techniques such as differential phase measurements in the X-band or polarimetric decomposition in the C-band. Although the Ku-band is considered optimal for penetrating snow and estimating SWE, it is not yet widely available on current satellite platforms (Rabatel et al. 2017).

Snow depth can be assessed using in-situ data - such as meteorological stations data -, snow models, such as CROCUS or SNOWMODEL, or satellite datasets such as Copernicus Global Land Service – Snow Depth (Yu 2021).

Snow density, on the other hand, is typically derived from in-situ measurements or estimated through physical or empirical modeling approaches. The best approach to modelized it is an empirical models based on snow age, temperature and humidity density (Lee et al. 2024). As any in situ measurements were done back in 2018, a more basic approach was favored in this study.

Snow Cover

Numerous snow models are available in literature. Table 1 summarizes the key characteristics of the models considered in this study. Given the small size of the watershed, the need for a short temporal resolution and a high spatial resolution, the two Copernicus Wet/Dry Snow and SAR-WET SNOW products could be used. These datasets provides 6 – 12 days estimates of wet and dry snow at a spatial resolution of 60 meters, which is particularly useful for estimating snowmelt (« Wet/Dry Snow 2016-Present (Raster 60 m), Europe, Daily », s. d.; « SAR Wet Snow 2016-Present (Raster 60 m), Europe, Daily », s. d.). In another

hand, despite the great temporal resolution of the MODIS/TERRA model, Snow Cover Daily L3, the spatial resolution is too big to provides consistent results on such a little basin (Hall et Riggs 2016). The Theia snow cover model uses data from Landsat 8 (30 x 30m, 16 days) and Sentinel-2B (20 x 20 m, 6-12 days). Therefore, it lowers the temporal resolution and the median frequency of revisiting is 2,9 days (Gascoin et al. 2019). Furthermore, a recent study from Unige highlights a new algorithm of Snow Observation from Space (SOfS) for snow cover in Switzerland (Poussin et al. 2025). This dataset has a 30 m resolution with a monthly temporal resolution.

Name of the model	Agency	Spatial resolution	Temporal resolution
WET/DRY SNOW	Copernicus	60 m x 60 m	6-12 days
SAR-WET SNOW	Copernicus	60 m x 60 m	6-12 days
Snow Cover daily L3	MODIS/TERRA	500 m x 500 m	daily
Data Terra	Theia snow cover	30 m x 30 m – 20 m x 20 m	2,9 days (median)
SOfS algorithm	Unige	30 m x 30 m	monthly

Table 1: Overview of the different models

The *SOfS* algorithm was chosen for this appliance, due to its parametrization made especially for Switzerland, this product offers a great accuracy. Other remote sensing methods, such as optical snow cover mapping (e.g., MODIS, Theia, Copernicus) and lidar-based elevation change detection (e.g., ICESat-2), are acknowledged but are not the primary focus of this study. Instead, they are considered complementary sources for potential future validation or multi-sensor fusion.
For example, the presence of wet snow is a strong indicator of ongoing snowmelt and thus provides a valuable proxy for estimating SWE dynamics, particularly in small alpine watersheds where snowmelt timing is critical for hydrological modeling. The high spatial and temporal resolution of the Copernicus product makes it especially suitable for this application.

Snow depth

The Theia snow products offer a snow depth model, unfortunately, during the period of this study, the model was momently unavailable. Radar sensors can be used to estimate snow depth, while LiDAR systems provide high-precision measurements of surface elevation changes, which can be used to infer snow accumulation (Niang et al. 2006). Such an approach requires a lot of preprocessing to assess the errors involved by trees, bushes and other elements of the landscape. Therefore, a more basic approach was chosen, using R to perform daily spatial interpolation of snow depth over a defined study area for the year 2018 using a Random Forest regression model.

Snow density

Unfortunately, no product offers a snow density map with a small resolution as required. Models for snow density are hard to use due to the need for in-situ measurements, such as snow age. These values must be measured directly in the field. As no such data were acquired during Ordòñez field trip in 2018, a simplified parametrization was selected. First possibility is to use average values (Lee et al. 2024). Newly fallen snow typically has a density ranging from 20 to 300 kg·m^{-3}, depending on factors such as temperature, wind, and precipitation type. Dry snow under calm conditions has a density of 60–120 kg·m^{-3}, but this increases significantly in the presence of wet snow, sleet, or strong winds, which fragment snow particles and enhance compaction (Jordan 1999). Another method could be to use a parametrization using air temperature (Pomeroy et Brun 2001) (Fig. 4, Equ. 3)

$$\rho_{Snow} = 67,9 + 51,25e^{(T/2,59)} \quad (3)$$

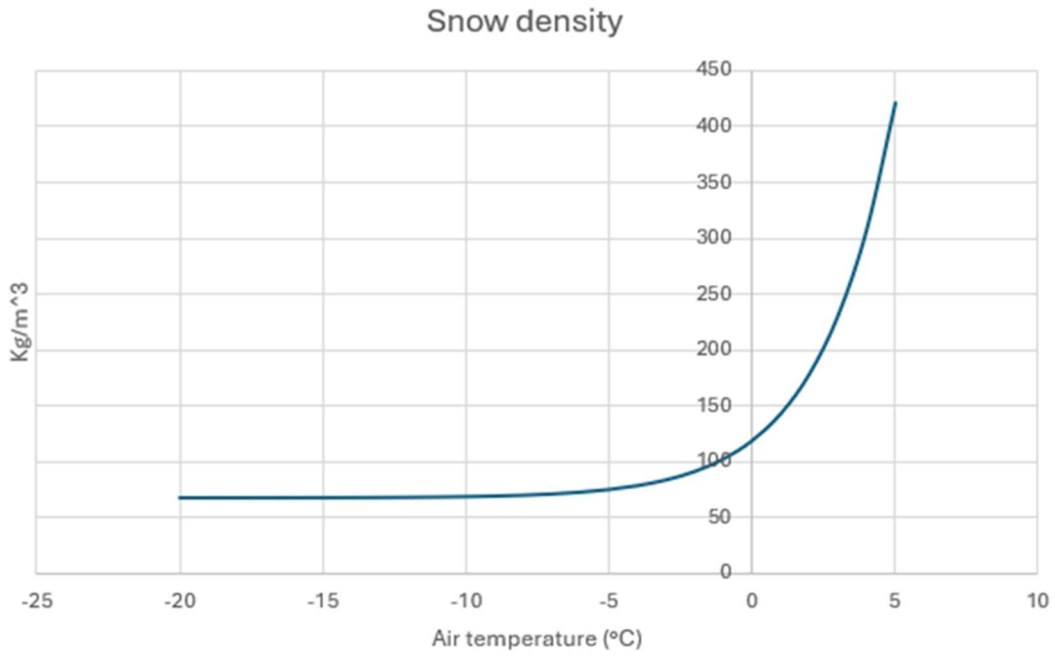

Figure 4: parametrization of the snow density using air temperature (Pomeroy et Brun 2001)

Study site

Lac de Bretaye (46°19'34.5" N, 7°4'18.9" E, Fig. 5) is located at 1785 m.s.l. in Switzerland, Canton de Vaud. It is a small and shallow hypereutrophic and pre-alpine lake, with a maximum depth of ~ 9 m and a surface area of ~ 4 ha (Ordóñez, 2022). The lake is surrounded by meadows used for animal grazing, except for the south where Alnus viridis proliferate (Thöle et al., 2016). In the summer of July 2019, abundant macrophytes were found on every side of the lake except the east side. The lake is surrounded by a cirque with high and steep slopes on the north and west side of it. Lac de Bretaye doesn't have any surface upstream and downstream flows (Ordóñez, 2022).

Lac de Bretaye is in the pre-Alpine region of Ollon (Vaud, Switzerland), near Lac des Chavonnes and Lac Noir, approximately 500 m apart and with an elevation difference of 50 to 100 m. A tracer study indicated that at least Lac de Bretaye and Lac Noir contribute to the same two groundwater tables: Le Poutet (Ollon) and Coussy-Loudze (Leysin) (Parriaux, 1997).

Figure 5: Lake Bretaye, Switzerland, VD (46°19'34.467" N, 7°4'18.89" E)

The basin is small, with a total area of approximately 3 km^2. The subbasins area of Bretaye, Chavonnes and Noir are respectively 1.36, 1.04 and 0.62 km^2 (Fig. 6).

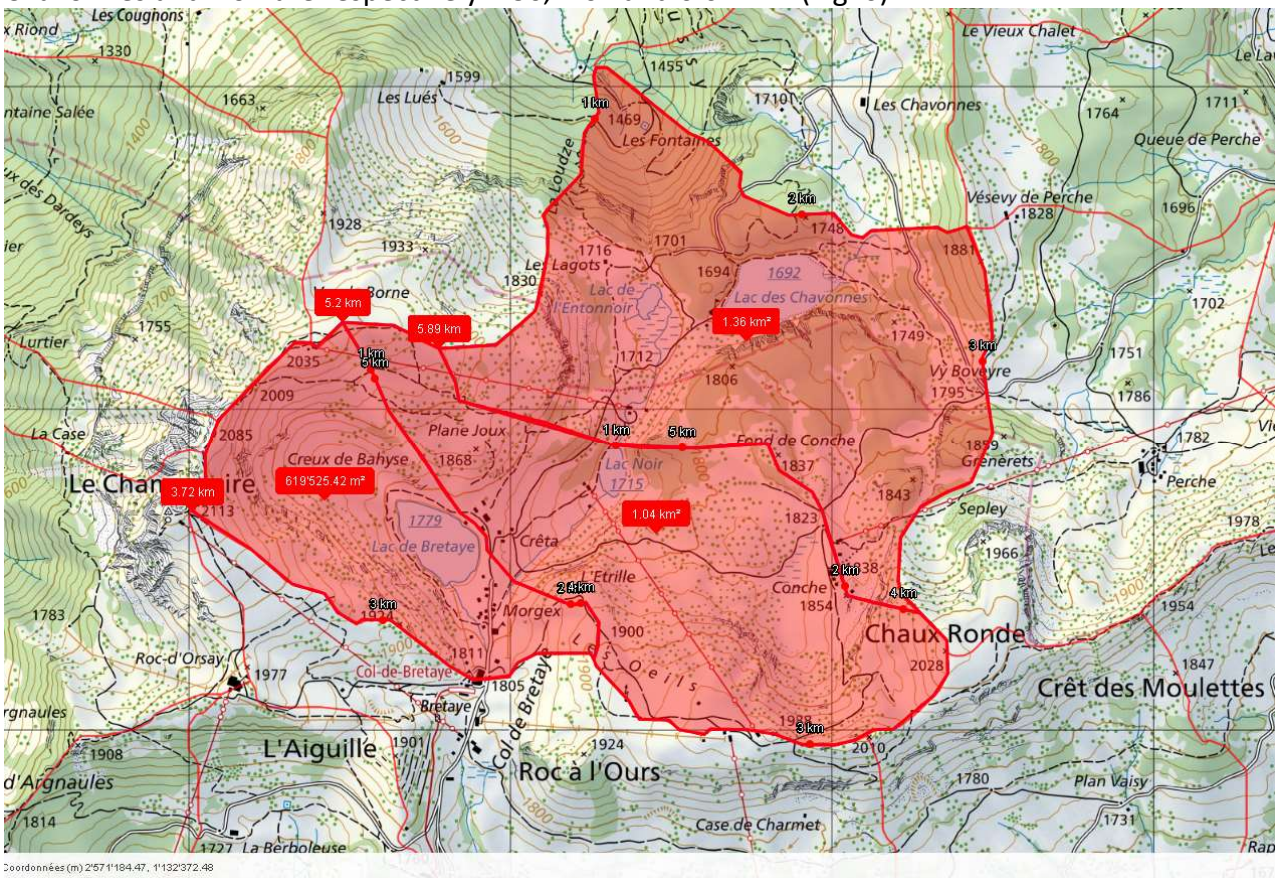

Figure 6 : areas of the 3 watersheds estimated with swiss topographic data (OFEV 2024)

Geology of the watershed

Lac de Bretaye follows a nivo-pluvial regime, with water level variations primarily driven by snowmelt and, to a lesser extent, rainfall (Parriaux 1997). The lakebed is semi-permeable (Parriaux 1997) (Fig. 7). As the field trip took place between June and September 2018, it started at the end of the snowmelt season. Consequently, the lake level was expected to stabilize following the final snowmelt events and thereafter respond mainly to rainfall.

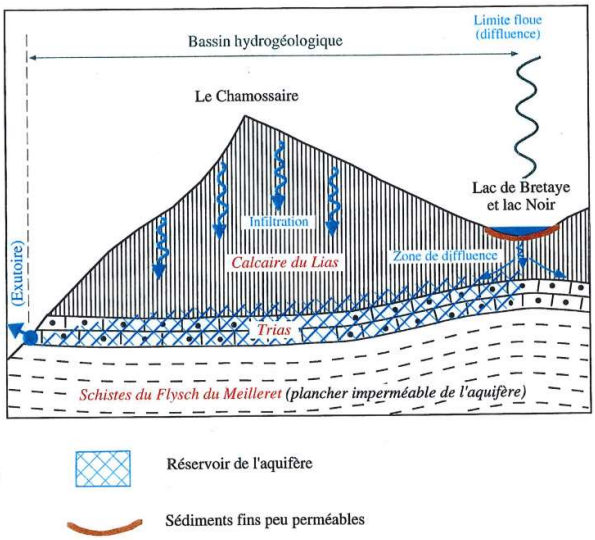

Figure 7: Hydrogeological structure of the aquiferous of Le Poutet (Parriaux, 1997)

At the beginning of the field campaign in late June 2018, snow patches were still present within the catchments (Ordóñez 2022). The three lakes are surrounded by fracture systems (red lines, Fig. 8) (« Cartes de la Suisse - Confédération suisse - map.geo.admin.ch », s. d.). Lac de Bretaye lies within a dejection cone (light yellow, Fig. 8) composed of silt, gravel, and sand. Such deposits in topographic depressions typically form lakes, as their semi-permeable nature hinders rapid drainage. Red dotted lines on the map indicate the boundaries of an ancient torrent. Geologically, the area is part of “La lame d’Oudioux,” a complex rock structure with surface layers comprising distinct geological units. The pink unit (Fig. 8) corresponds to a karstified Lower Jurassic limestone formation, representing a major aquifer. In contrast, the brown unit represents Aalenian black nodule-bearing schists, a clay-rich and poorly permeable formation.

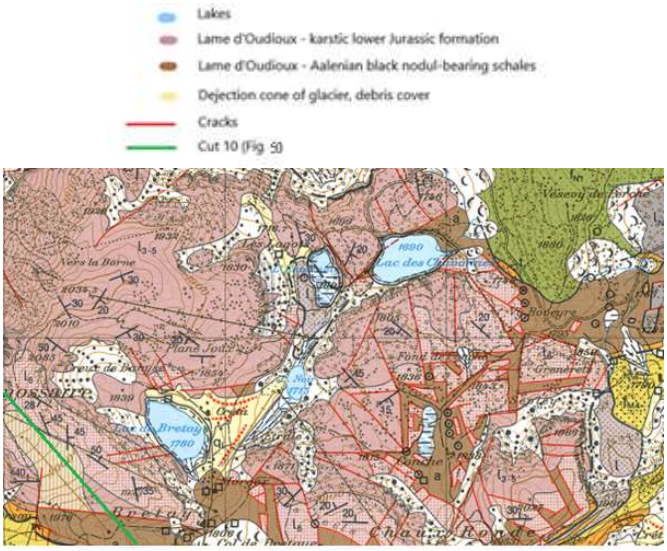

Figure 8: Swiss Geological Atlas, scale: 1:25000, (Swisstopo 2024)

Beneath these formations, a thin stratigraphic layer separates the upper portion of the “lame d’Oudioux” from the Meilleret Flysch (white dotted line, Fig. 9). The Flysch is a thick, permeable unit that supports the Le Poutet groundwater table. The intervening layer comprises Rhaetian sandstones—permeable due to their granular structure—and siliceous dolomites, which exhibit fissure permeability. Both formations are generally attributed to the Triassic period.
The right portion of cross-section 10 (Fig. 9) corresponds to the green line shown in both Figures 8 and 9.

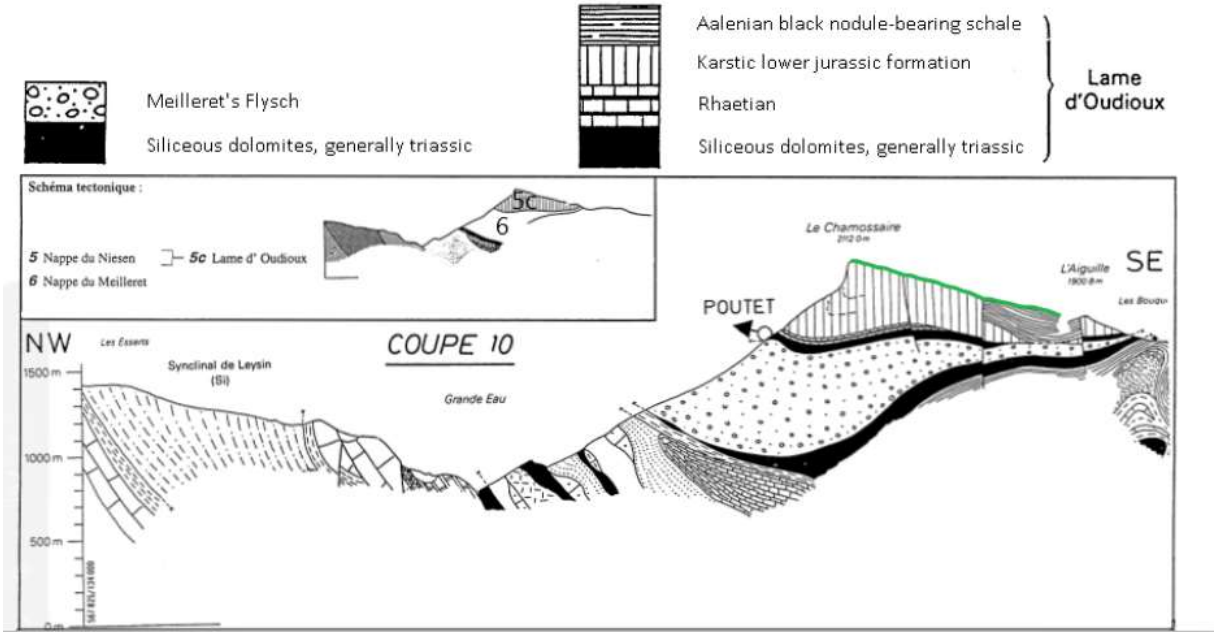

Figure 9: Geological cut of the Bretaye zone, from the Swiss Geological Atlas, sheet 1285 scale: 1:25000(Swisstopo 2024)

Methodology

Watershed delineation

The first step involved delineating the study area to ensure that all subsequent analyses were spatially constrained to the relevant region. To achieve this, we downloaded the "Swiss Watersheds" dataset in .gdb format from the official website of the Swiss Federal Office for the Environment (OFEV 2024). Using ArcGIS Pro, the specific watershed of interest was extracted and exported as a shapefile. After verifying the spatial reference system to ensure consistency with Sentinel-2 imagery, the dataset was ready for further geospatial processing.

Snow cover

In this study, a direct remote sensing approach based on the *SOfS* algorithm product was adopted. This model will provide information about snow cover with an accuracy of ~95% and an overall acceptable temporal resolution, with a 30 m spatial resolution. This layer is the boundary one in terms of temporal resolution. Therefore, other layers were acquired daily and monthly snow cover maps were used for the whole month variability of snow density and snow depth.

The *SOfS* algorithm is a remote sensing method developed within the Swiss Data Cube (*SDC*) to monitor snow cover across Switzerland using optical satellite imagery. It addresses the challenge of cloud obstruction by applying a structured seven-step gap-filling process that enhances data continuity and reliability.

At its core, *SOfS* algorithm generates monthly composites by selecting the maximum *NDSI* per pixel, effectively reducing cloud interference. Seasonal aggregation further improves data quality, resulting in up to 88% cloud-free observations.

The algorithm integrates data from multiple satellite missions—Landsat-5, Landsat-7, Landsat-8, and Sentinel-2—to reduce cloud-related gaps. Additional steps include spatial filtering, neighborhood analysis, and elevation-based reclassification, which improve snow detection in mountainous regions.

Validation against in-situ snow depth measurements confirms high accuracy, exceeding 95% when using a 5 cm threshold. While monthly resolution may miss short-lived snow events, especially in transitional elevation zones, *SOfS* provides robust long-term snow cover data suitable for climate monitoring and trend analysis.

Implemented in Python, the algorithm is scalable and adaptable to other regions with similar environmental conditions, offering a reliable tool for large-scale snow dynamics assessment.

Snow density

This study employs a geospatial modeling approach to estimate daily snow density across a defined watershed using temperature data from meteorological stations and a DEM. The methodology integrates spatial interpolation, regression modeling, and raster-based computation within the R programming environment, leveraging the terra, sf, and tidyverse packages.

Three primary datasets were used:

- A digital elevation model (DEM) at 25-meter resolution, representing terrain elevation.
- A polygon shapefile delineating the watershed boundary
- A series of daily mean temperature CSV files (temp_YYYY_MM_DD.csv) containing point measurements with geographic coordinates and temperature values.

10 weather stations surrounding the watershed were retained for this appliance (Table 2), and data was acquired on the *météo suisse* open data portal (« Open Data - MétéoSuisse », s. d.).

Station	Acronym	Latitude [°]	Longitude [°]
Diablerets	DIA	46,32675	7,20378
Aigle	AIG	46,32665	6,92447
Chateau d'Oex	CHD	46,47982	7,13966
Evionnaz	EVI	46,18295	7,02675
Sion	SIO	46,21865	7,33020
Col-Des-Mosses	CDM	46,39153	7,09824
Bouveret	BOU	46,39345	6,85701
Moléson	MVE	46,29881	7,46081
Montana	MLS	46,54620	7,01775
Adelboden	ABO	46,49170	7,56070

Table 2: Overview of weather stations used for temperature maps

The use of high-resolution *DEM* data is critical for accurate terrain modelling (Al-Mutairi et al. 2019) because interpolation method applied to *DEM* significantly influence the precision of derived environmental variables. The *DEM* (Swisstopo 2004) was loaded using the terra::rast() function, and the watershed polygon was imported and reprojected to match the *DEM*'s coordinate reference system using sf::vect() and terra::project().

The algorithm iterates over each day of the year (1–365), corresponding to the year 2018. For each day, the script constructs the date string and locates the corresponding CSV file containing temperature observations.

If the file is missing or malformed (e.g., missing required columns), the iteration is skipped with appropriate logging.

Valid temperature data are converted into a spatial object and reprojected to the DEM's coordinate system. The elevation at each station location is extracted from the DEM using terra::extract(). These altitude values are appended to the station dataset.

A linear regression model is fitted to predict temperature as a function of altitude (Equ. 6) (Wang et al. 2011). Effectively, particularly in mountainous regions, surface air temperature exhibits a strong dependance on altitude.

$$T_{air} = \beta_0 + \beta_1 \times Altitude \qquad (6)$$

This model captures the lapse rate effect, where temperature typically decreases with elevation. If the regression fails (e.g., due to insufficient data), the day is skipped.
A regular grid with 20 m resolution is generated over the DEM extent. Using the fitted regression model, temperature values are predicted for each grid cell based on its elevation. The predicted temperature raster is then masked to the watershed boundary using terra::mask().
Snow density is computed for each grid cell using an empirical exponential model, following Equation 3 (Pomeroy et Brun 2001).
This formula reflects the inverse relationship between temperature and snow density, assuming colder temperatures yield lighter, less dense snow.
The resulting snow density raster is exported as a GeoTIFF file using terra::writeRaster(). Each file is named according to the date and stored in the designated output directory. Errors during export are logged but do not interrupt the loop.

Snow depth

The R code used to infer snow depth integrates fixed topographic variables (elevation, slope, aspect) and dynamic meteorological data (temperature, wind speed) with observed snow depth measurements from Excel files. For each day, the script preprocesses and spatially transforms the snow station data, extracts environmental predictors from raster layers, trains a Random Forest model, and applies it to a prediction grid constrained by a watershed mask. The resulting interpolated snow depth raster is then exported for each valid date, enabling high-resolution spatiotemporal analysis of snow distribution.
Weather stations were used depending on the availability of the different variables needed and the spatial distance to the study site, a summary of the stations used is available on table 3. Table 4 summarizes the stations where snow depth data were acquired.

Station	Acronym	Latitude [°]	Longitude [°]
Sion	SIO	46,21865	7,330203
Evionnaz	EVI	46,18295	7,026747
Visp	VIS	46,3029	7,842958
Moléson	MLS	46,5462	7,017753
Adelboden	ABO	46,4917	7,560703
Vevey	VEV	46,47124	6,815056
Montagnier, Bagnes	MOB	46,07102	7,225272
Château d'Oex	CHD	46,47982	7,139656
Evolène	EVO	46,11221	7,508631
Col des Mosses	CDM	46,39153	7,098239

Table 3: Overview of weather stations used for dependent variables maps (except temperature).

Station	Acronym	Latitude [°]	Longitude [°]
Diablerets	DIB	46,32675	7,203781
Gryon	GRY	46,2748	7,060363
Grimentz	GRI	46,17998	7,578081
Hérémence	HER	46,17829	7,404389
Sierre	SRE	46,29703	7,550214
Zweisimmen	ZWE	46,48819	7,532022
Jaun	JAU	46,61157	7,275894
Fruence	FRC	46,52583	6,901847
Saas Balen	SBA	46,15501	7,939382
Tour de Gourze	TDG	46,51034	6,740947

Table 4: Overview of weather stations used for snow depth dataset

The temperature kriged maps acquired for snow density were used. *TPI*, slope and aspect maps were created directly using the *DEM*.
For each day, meteorological station data (latitude, longitude, wind speed and wind direction) are extracted from Excel files, cleaned, and transformed into spatial vectors using the LV95 coordinate system. Wind vector components (u and v) are computed trigonometrically. These spatial points are enriched by extracting topographic variables—elevation, topographic position index (*TPI*), slope, and aspect—from fixed raster layers. The enriched dataset is then used to fit two linear regression models, one for each wind component. These models are applied to a regular prediction grid covering the study area, enabling spatial prediction of wind speed and direction.

Snow Water Equivalent

The resulting layer was derived through pixel-wise multiplication of three raster datasets: snow cover, snow depth, and snow density. Due to discrepancies in spatial resolution among the input layers, a resampling procedure was applied to achieve a harmonized resolution of approximately 28.2 m. The snow cover dataset encodes four categorical values: NA for water bodies, 0 for snow-free pixels, 1 for snow-covered pixels, and 2 for cloud-covered pixels. In the computational implementation, only pixels with a snow cover value of 1 were retained for multiplication; all other values were assigned zero to exclude non-snow-covered areas. Given that snow density is expressed in kilograms per cubic meter [kg / m³], the output of the multiplication yields the mass of snow per pixel (in kg), which can be converted to volume [m³] using the density of water at 0 °C (melting point) as a reference.
Subsequent to the raster-based estimation of snow water equivalent (*SWE*), a daily summation of the pixel values was conducted to quantify the total volume of water [m^3] across the study area. These aggregated values were exported to a *CSV* file, serving as a temporal dataset for further analysis. This file was then utilized to generate graphical representations illustrating the temporal evolution of *SWE*-derived water volume throughout the observation period.
Finally, to infer the SWE over the watershed of Bretaye, smaller than the whole basin, a simple factor has been used, referring to surface ratio between the Bretaye basin (~0,62 km^2) and the whole watershed (~3,02 km^2) (Fig.6). The whole methodology is reviewed on the following figure (10).

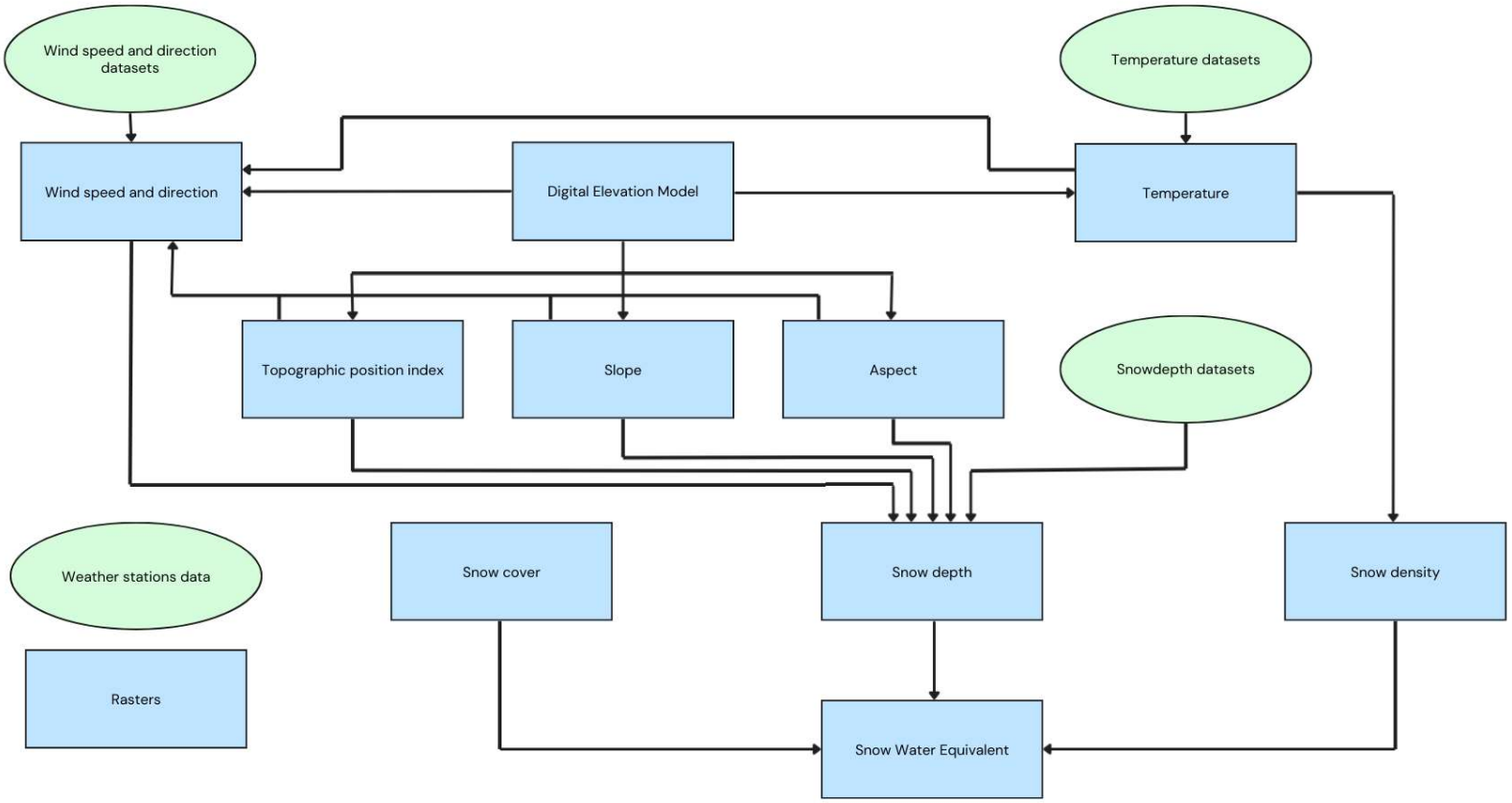

Figure 10: Schema reviewing the methodology and the different explicative variables

Results

Dependent variables

As kriging method required to have all the data points within the kriged area, the dependent variables maps were first calculated over a bigger square area, including the weather stations, and afterwards the final products were cropped over the Bretaye Basin.

Wind speed and direction

Wind speed and direction were modeled using topographic variables—Topographic Position Index (TPI), slope, aspect, and Digital Elevation Model (DEM)—as predictors. The results indicate that wind speed generally increases along topographic aretes, suggesting that slope, aspect, and elevation exert a significant influence on wind speed variability. It is important to note that TPI, slope, aspect, and DEM are static variables, remaining constant throughout the study period, whereas wind speed and direction are dynamic and vary temporally. Figure 11 illustrates the wind speed observed on January 1st, 2018. Due to unidentified technical issues, the wind direction raster datasets were rendered unusable and subsequently excluded from the analysis. Despite multiple attempts, the integrity and accessibility of these files could not be restored, preventing their integration into the modeling framework.

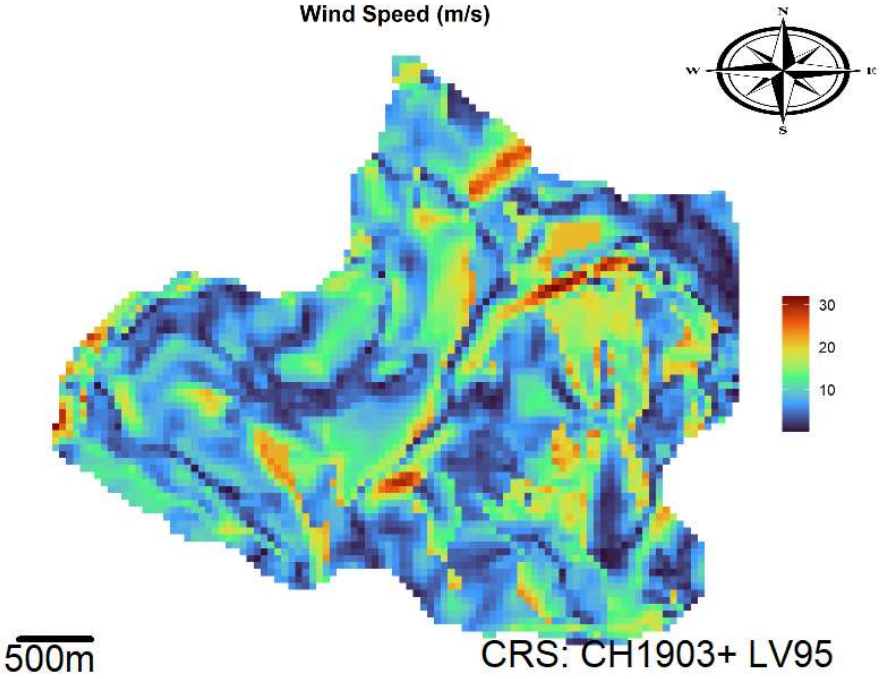

Figure 11: Wind speed map on 01.01.2018

Temperature

Temperature maps were derived using a *DEM*, and the resulting spatial distribution closely mirrors the elevation variability across the study area. On January 1st, 2018, (Fig. 12) temperatures in the lowest part of the basin were approximately 0 °C, whereas the highest point—Le Chamossaire—recorded temperatures near −3 °C. This gradient is consistent with the elevation difference of approximately 600 meters between the lowest and highest points of the watershed. The observed pattern aligns with the standard environmental lapse rate in alpine regions, where temperature typically decreases by approximately 0.56 °C per 100 meters of elevation gain (Rolland 2003).

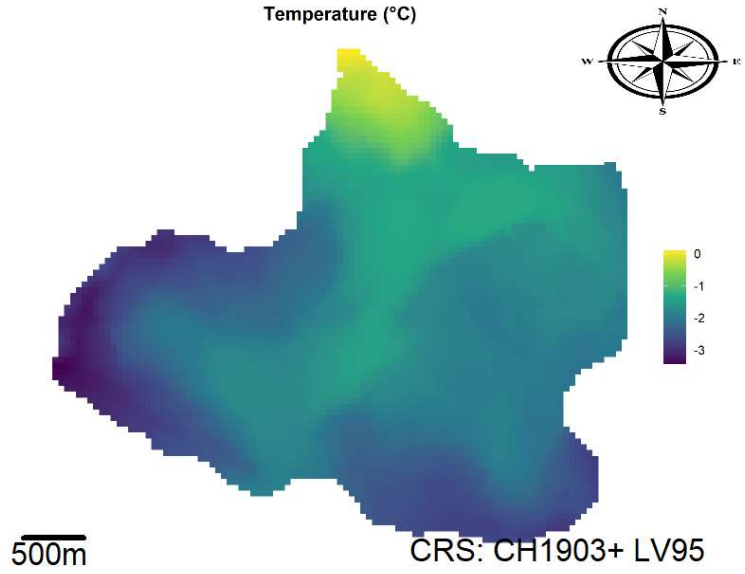

Figure 12: Temperature map on 01.01.2018

TPI, slope, DEM and aspect

The aspect map (Figure 13) clearly illustrates a division of the watershed into two distinct sections, with the central boundary corresponding to the valley floor. The western slope, predominantly displaying blue tones, and the eastern slope, characterized mainly by yellow tones, reflect contrasting orientations. Despite this general division, both sides exhibit notable spatial heterogeneity in aspect, indicating variations in slope orientation within each section of the valley.

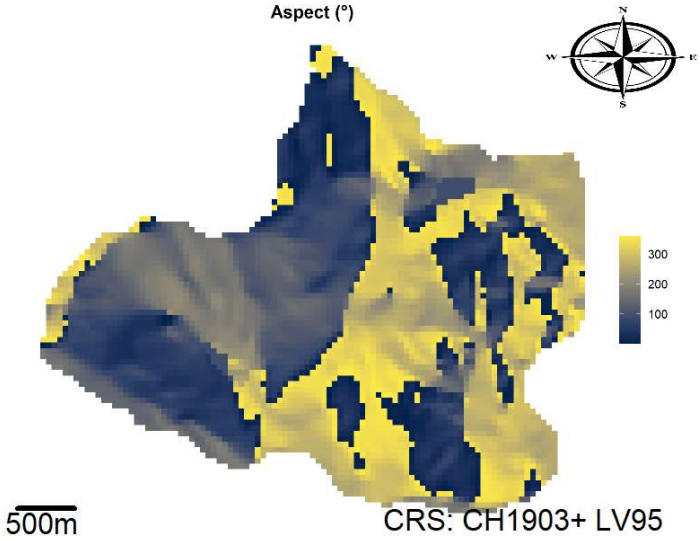

Figure 13: Aspect map

The Digital Elevation Model (DEM) (Fig. 14) effectively captures the altitudinal variation within the basin, highlighting its topographic features such as ridgelines, peaks, and valley floors. This representation provides essential insight into the basin's geomorphology, delineating elevation gradients that influence a range of environmental processes, including hydrology, microclimate, and vegetation distribution. Enhancing the analysis by integrating derived topographic indices—such as slope, aspect, and curvature—could further improve the interpretation of terrain-related dynamics.

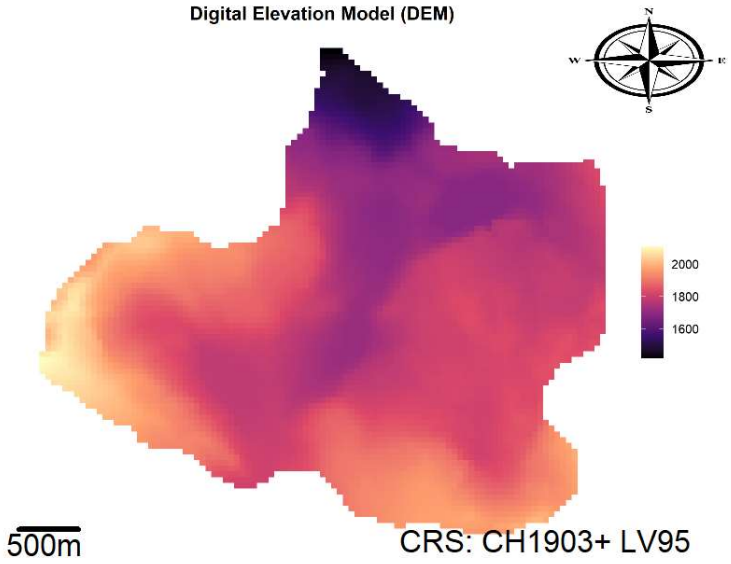

Figure 14: DEM

The slope map (Fig. 15) reveals significant variability in terrain steepness across the watershed. Certain regions exhibit steep slopes exceeding 50°, particularly along ridgelines and aretes, while other areas—such as the valley floor—are characterized by relatively flat terrain. This spatial distribution effectively delineates key topographic features, including steep escarpments and flatter depositional zones. Additionally, the slope map helps to identify geomorphological elements such as aretes and lake basins, which are typically associated with sharp slope transitions or low-gradient areas. Incorporating this information is crucial for understanding landscape stability, hydrological flow paths, and potential erosion processes within the watershed.

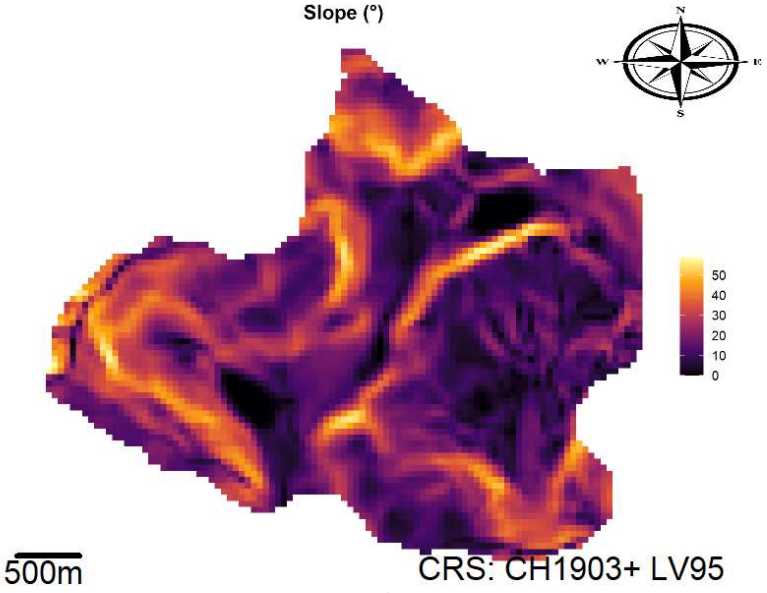

Figure 15: Slope map

TPI (Fig. 16) is a dimensionless index that measures the difference in elevation between a specific cell and the average elevation of its surrounding neighborhood. Positive values indicate elevated features (e.g., ridges, hilltops), values near zero represent flat or mid-slope positions, and negative values indicate depressions or valleys. This makes TPI particularly useful for identifying and classifying landforms across a landscape, especially when used in conjunction with slope and curvature data.

TPI map shows a strong spatial correlation with the slope map, particularly in the identification of key landforms. Aretes typically exhibit high positive TPI values, around +10, indicating that these features stand significantly above their immediate surroundings. In contrast, the valley floor shows TPI values close to 0, representing terrain that is relatively level compared to neighboring areas. Interestingly, areas adjacent to aretes sometimes display negative TPI values, around −5, corresponding to concave or recessed topographic positions such as hollows or depressions along steep slopes.

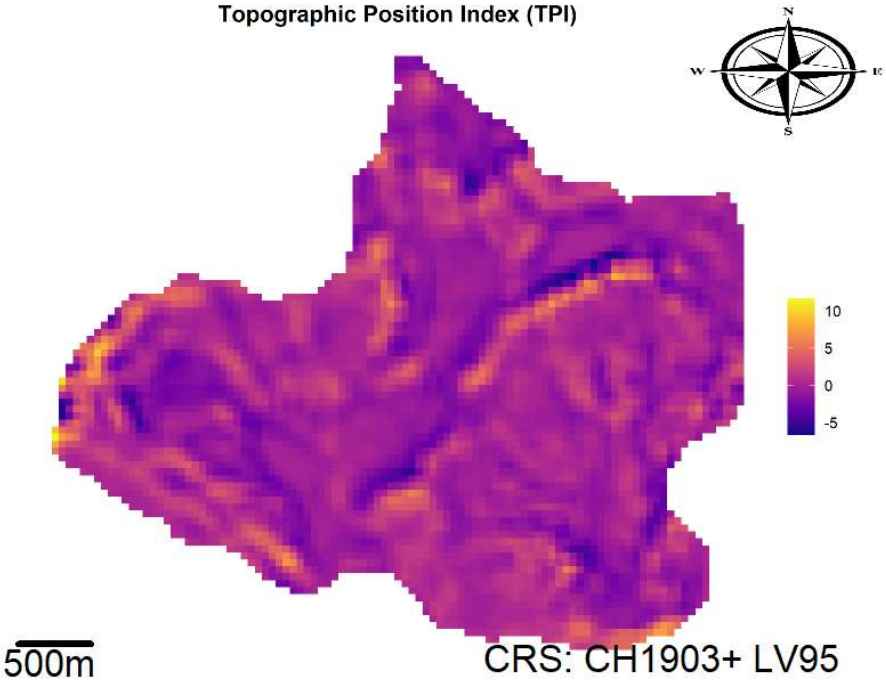

Figure 16: TPI map

Snow density

The snow density map dated 01 January 2018 (Fig. 17) exhibits a clear spatial correlation with the digital elevation model (*DEM*), which served as the primary explanatory variable in the generation of temperature maps. These temperature maps were subsequently employed to estimate snow density using the parametrization proposed by Pomeroy (2001). The resulting density values fall within the expected range for dry snow, consistent with the ambient temperature conditions recorded on that day, which varied between 0°C and −3°C.

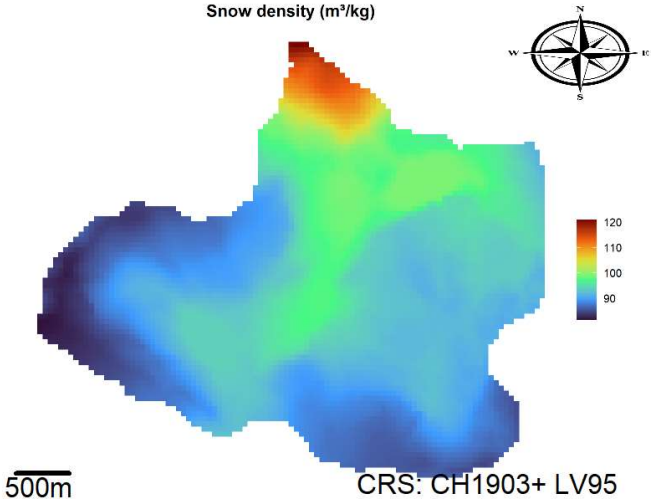

Figure 17: Snow density map of the watershed on 01.01.2018

Snow depth

The snow depth map from 01 January 2018 (Fig. 18) highlights the influence of multiple explanatory variables used in its derivation. A distinct delineation across the watershed reflects the impact of aspect, while the observed spatial variability suggests a complex interplay between slope, wind speed, and topographic position index (TPI). Snow depths range from 31 to 48 cm, which aligns well with measurements from nearby weather stations: Sion (~500 m elevation) recorded 10 cm, and Les Diablerets (~2900 m) recorded 48 cm. Given that the watershed lies between these two sites in terms of altitude, the estimated values are consistent and plausible. The broader range observed within the watershed is likely attributable to its more intricate topography compared to the relatively simpler terrain surrounding the weather stations.

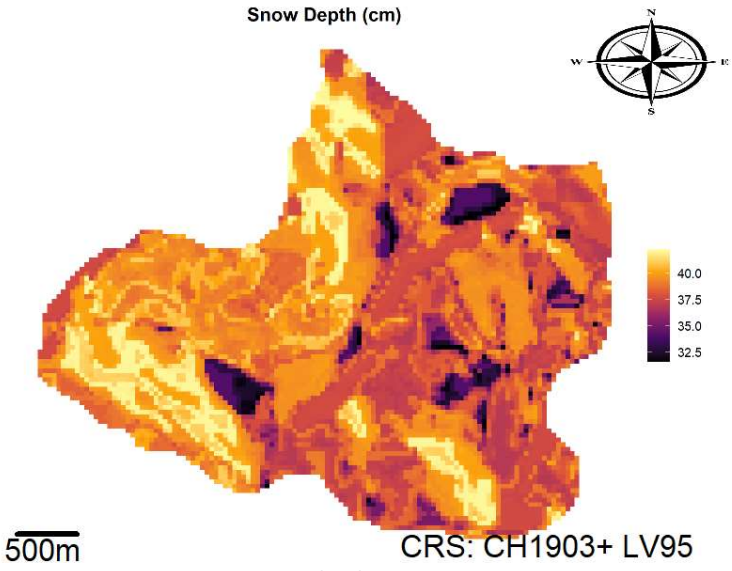

Figure 18: Snow depth map on 01.01.2018

Snow water equivalent

The snow water equivalent (SWE) map dated 01 January 2018 (Fig. 19) reveals a key limitation of the modeling approach: the presence of cloud cover. Pixels obscured by clouds were systematically assigned a SWE value of zero, despite the high likelihood of underlying snow cover. This simplification was adopted to maintain consistency and enhance the reliability of the dataset. Excluding these cloud-covered areas, SWE values across the domain ranged from 25,000 to 40,000 kg, which aligns with expected magnitudes based on prior observations. Given the spatial resolution of 28.2 meters, a representative snow depth of 0.5 meters, and a snow density of 80 kg/m³, the estimated SWE volume is consistent with an order of magnitude of approximately 32,000 kg per pixel.

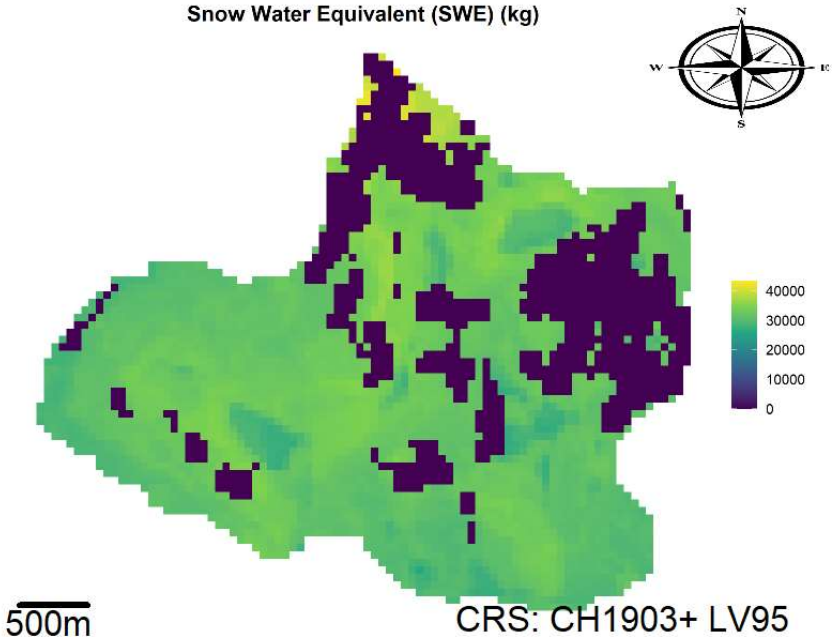

Figure 19: Snow water equivalent on 01.01.2018

Temporal evolution of SWE

The temporal evolution of snow water equivalent (SWE) (Fig. 20), expressed in cubic meters of water, reveals notable seasonal patterns. Specifically, it highlights the two distinct snow seasons of 2018. The 2017–2018 snow season concluded on April 18, with minor snow inputs continuing until May 14. The 2018–2019 season began on December 8, preceded by small accumulations starting on October 28. To compare SWE between the entire watershed and the Bretaye basin, a scaling factor of 0.205 was applied, reflecting the ratio of their respective surface areas. Significant variability is observed, particularly toward the end of the 2017–2018 season, when snow tends to become wetter and denser, influencing SWE measurements.

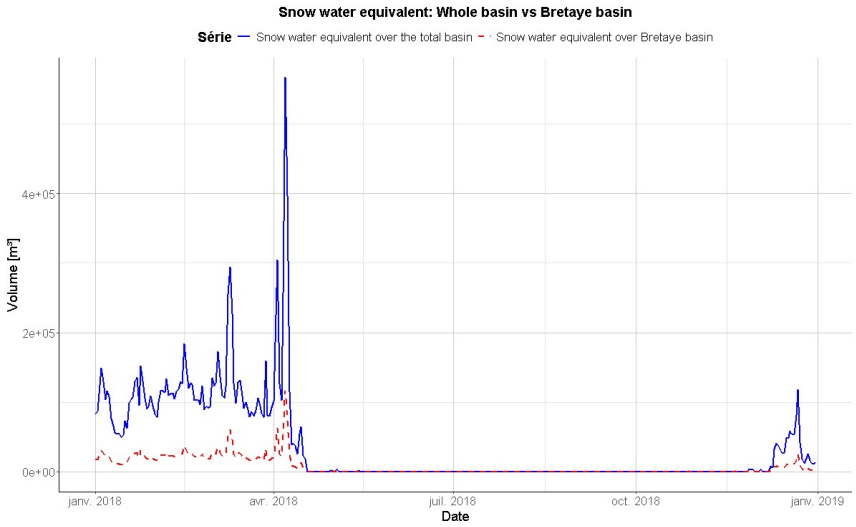

Figure 20: SWE between Bretaye and the whole basin

The monthly variability of snow water equivalent (SWE), shown on the right axis, and the water mass balance, on the left axis, reveals a tenfold difference in magnitude (Fig- 21). Notably, the water level of Lake Bretaye exhibited increased variability during June, indicating a net decrease in water level. This decline is attributed to snowmelt, which was expected during this period. Between the last recorded instance when SWE was not zero and the start of the 2018 field campaign, one month and five days had passed. If considering the last moment before SWE dropped to zero, the gap extends to approximately two months prior to the field trip. These intervals will be discussed in the discussion chapter.

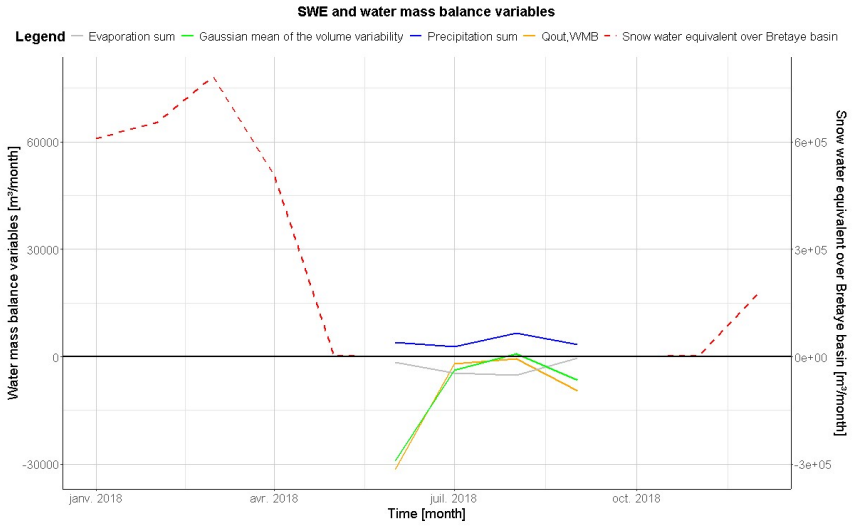

Figure 21: SWE over Bretaye (right axis) and water mass balance variables (left axis)

Discussion

The spatial analysis of the Bretaye Basin highlights the strong influence of topography on key environmental variables. The use of kriging necessitated initial interpolation over an extended domain encompassing all weather stations, followed by cropping to the basin boundaries, ensuring comprehensive spatial coverage. Wind speed exhibited a clear topographic control, generally increasing along aretes, consistent with the roles of slope, aspect, and elevation in modulating local airflow patterns; however, wind direction data could not be integrated due to technical limitations. Temperature distributions closely mirrored the DEM, with a decrease of approximately 3 °C between the lowest and highest elevations, reflecting the expected alpine lapse rate. The aspect, slope, DEM, and TPI maps revealed pronounced heterogeneity, delineating geomorphological features such as ridgelines, valleys, and aretes, and emphasizing the utility of TPI in identifying elevated and recessed landforms. Snow accumulation patterns were similarly influenced by topography: snow density correlated strongly with elevation, while snow depth was shaped by the interplay of aspect, slope, and TPI, yielding values consistent with nearby station measurements. The SWE map highlighted methodological constraints, particularly the assignment of zero values to cloud-obscured pixels, yet the derived SWE magnitudes were broadly in agreement with expectations.

Firstly, it is important to address the quality of the explanatory layers of SWE calculated in this study. Snow density varies according to numerous factors, including air temperature, wind speed, wind direction, solar radiation, aspect, and precipitation in the form of snow or rain. The parameterization based solely on temperature is therefore very minimal in terms of precision. Moreover, the temperature map used as input does not account for wind speed or direction, but only for elevation. Wind patterns are commonly observed in the Swiss Alps, notably the Foehn—a warm wind blowing from the south, often persisting for several consecutive days. Additionally, snow “ages” and tends to densify, either through melting or compaction. To account for this, researchers generally rely on in-situ measurements to calibrate their models.

As with snow density, the lack of in-situ data does not allow for quantitative validation of these variables. Nevertheless, the order of magnitude reached appears reasonable. Snow depth was estimated using a more complex model, likely closer to reality than the snow density parameterization; however, the absence of wind direction, solar radiation, and snowfall / precipitation data also limits the model. These factors have a direct impact on snow depth and are neglected in this study.

The snow cover layer, in contrast, is highly accurate, though its 30 m resolution means that a pixel represents 900 m² on the ground. Consequently, if these 900 m² are only partially covered by snow, the *SOfS* algorithm is likely to classify the pixel as snow-free. This results in a probable early end-of-season estimate, as snow patches can persist for several weeks after the beginning of soil exposure in the Alps. Furthermore, although the cloud cover mask is well handled by the *SOfS* algorithm, it still generates NA values, which tend to underestimate SWE.

Figure 22 below presents several hydrological variables for Lake Bretaye. The blue curve represents precipitation over the lake, and the green curve shows the Gaussian mean of the lake's volume variability. These curves have similar amplitudes, whereas the yellow curve, representing precipitation over the watershed, shows a larger amplitude. This graph indicates that nearly all precipitation on the watershed infiltrates directly into the aquifer, as the lake level shows little response. Therefore, the meltwater from snow within the watershed likely follows the same dynamics. This behavior can be explained by the geological structure of the watershed, which is characterized by fissured porosity.

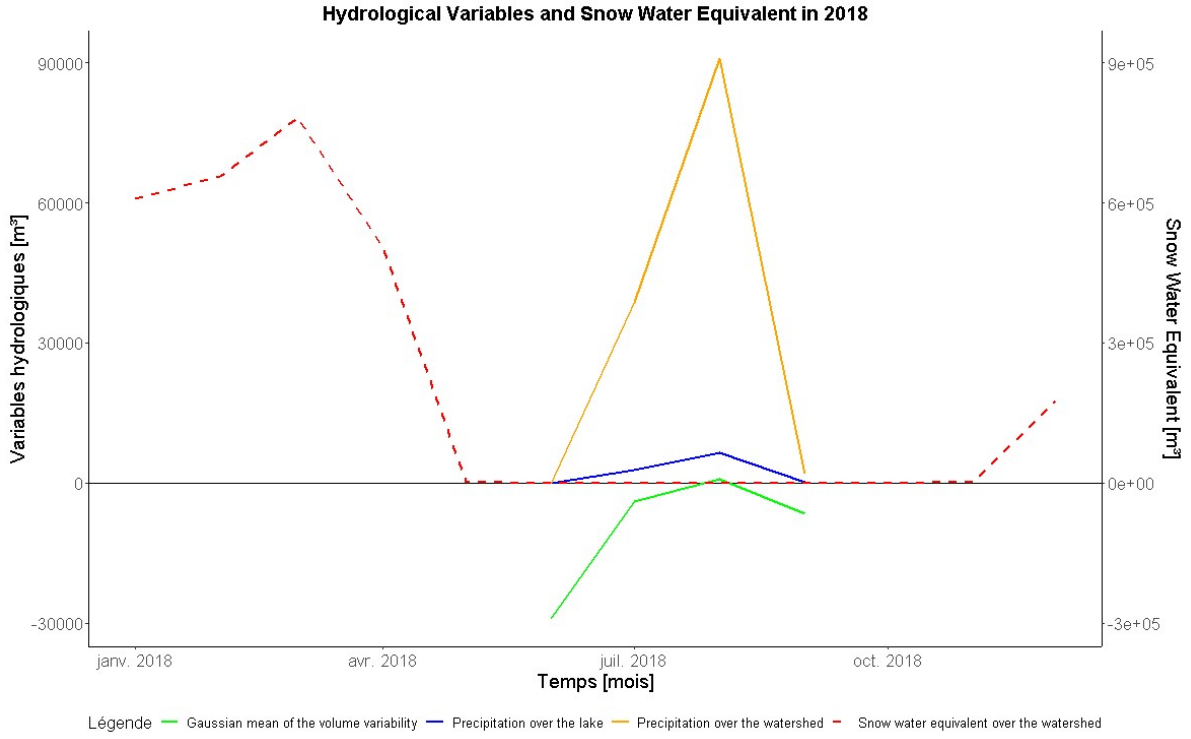

Figure 22: Precipitation over the watershed, the lake, gaussian mean of the volume variability and SWE

However, the amount of water stored in the snow is substantial, approximately an order of magnitude greater than summer precipitation. Considering the complex geological structure of the watershed, the large volume represented by this meltwater, and the probable underestimation of snow cover at the end of the season, it is likely that meltwater is responsible for the steep rise in lake level (green curve) observed in June. Indeed, this is probably residual meltwater, with the saturated aquifer and the flow through fractured rock contributing to a delayed response.

Overall, this study emphasizes the essential role of in-situ observations for the validation of spatial models. Snow processes are particularly challenging to parameterize accurately, and these results highlight that, without direct field measurements, modeling efforts can demand substantial computational time and storage resources while yielding limited practical accuracy. Consequently, it's recommended that comprehensive in-situ data collection be undertaken prior to large-scale modeling exercises to ensure both efficiency and reliability in snow-related environmental simulations.

Conclusion

This study aimed to enhance the understanding of hydrogeological processes governing alpine lake systems, with a particular focus on the seasonal dynamics driven by snowmelt and groundwater inputs. Using 2018 as a reference year—chosen for its compatibility with existing datasets from Ordóñez (2022)—the investigation pursued the following objectives: To characterize the transition between quickflow and baseflow hydrological regimes and assess their influence on lake water chemistry. To evaluate the role of snowmelt in modulating lake conductivity and nutrient availability, particularly during biologically active summer periods. To estimate groundwater contributions to lake volume and solute fluxes, using residual flow analysis derived from lake level, precipitation, and evaporation data. To identify potential unaccounted inflows, likely associated with snowpack dynamics, especially during early summer (June), when discrepancies in water balance were observed. By addressing these objectives, the study contributes to a more refined understanding of alpine lake hydrology and its implications for nutrient cycling and ecosystem functioning.

The spatial modeling of environmental variables across the Bretaye Basin revealed clear topographic influences on climatic and snowpack dynamics. Wind speed increased along ridgelines, shaped by slope, aspect, and elevation, though wind direction data were excluded due to technical issues. Temperature distribution followed elevation gradients, consistent with the expected lapse rate in alpine regions. Topographic indices (DEM, slope, aspect, TPI) effectively delineated geomorphological features such as aretes, valley floors, and escarpments, providing a robust framework for interpreting terrain-driven processes. Snow density and depth showed strong spatial variability, influenced by aspect, slope, and wind exposure, with modeled values aligning well with nearby station data. Snow Water Equivalent (SWE) estimates were consistent with theoretical expectations, though cloud cover introduced gaps in the dataset. Overall, the results confirm the reliability of the modeling approach and highlight the importance of integrating topographic and meteorological variables to understand alpine watershed dynamics.

This study confirms the strong influence of topography on environmental variables within the Bretaye Basin, with wind speed, temperature, and snow distribution all shaped by terrain features. However, several limitations emerged, notably the exclusion of wind direction data and the simplified parameterization of snow density based solely on temperature. The absence of key inputs—such as solar radiation, precipitation type, and in-situ measurements—limits the precision of snow-related models. The SWE layer, while broadly consistent with expectations, was affected by cloud cover and resolution constraints, likely leading to underestimations of late-season snow cover. Hydrological analysis suggests that most precipitation infiltrates directly into the aquifer, with delayed lake-level responses driven by residual meltwater and fractured bedrock flow paths. These findings underscore the need for robust field data to calibrate and validate spatial models. Future work should prioritize in-situ measurements and integrate additional meteorological variables to improve the accuracy and applicability of snowpack and hydrological simulations in alpine environments.

This study provides a foundational understanding of the spatial and hydrological dynamics within the Bretaye Basin, emphasizing the influence of topography on environmental variables and the challenges of modeling snow processes without in-situ data. While limitations remain, the results offer valuable insights into alpine watershed behavior and highlight key directions for future research, particularly the integration of field measurements to enhance model reliability and ecological relevance.

Bibliography

Al-Mutairi, Nawaf, Mohammad Alsahli, Mahmoud Ibrahim, Rasha Abou Samra, et Maie El-Gammal. 2019. « Spatial Enhancement of DEM Using Interpolation Methods: A Case Study of Kuwait's Coastal Zones ». *American Journal of Remote Sensing* 7 (1): 1. https://doi.org/10.11648/j.ajrs.20190701.12.

« Cartes de la Suisse - Confédération suisse - map.geo.admin.ch ». s. d. Consulté le 7 novembre 2024. https://map.geo.admin.ch/#/map?lang=fr&center=2572547.04,1131028.66&z=7.678&bgLayer=ch.swisstopo.pixelkarte-farbe&topic=ech&layers=ch.swisstopo.zeitreihen@year=1864,f;ch.bfs.gebaeude_wohnungs_register,f;ch.bav.haltestellen-oev,f;ch.swisstopo.swisstlm3d-wanderwege,f;ch.vbs.schiessanzeigen,f;ch.astra.wanderland-sperrungen_umleitungen,f;KML%7Chttps://public.geo.admin.ch/api/kml/files/0VWJeUYfSCepmvQGK8IEAQ;ch.bafu.wasser-teileinzugsgebiete_2&featureInfo=bottomPanel&catalogNodes=ech,532,614.

Dozier, Jeff. 1989. « Spectral signature of alpine snow cover from the landsat thematic mapper ». *Remote Sensing of Environment* 28 (avril): 9-22. https://doi.org/10.1016/0034-4257(89)90101-6.

Gascoin, Simon, Manuel Grizonnet, Marine Bouchet, Germain Salgues, et Olivier Hagolle. 2019. « Theia Snow Collection: High-Resolution Operational Snow Cover Maps from Sentinel-2 and Landsat-8 Data ». *Earth System Science Data* 11 (2): 493-514. https://doi.org/10.5194/essd-11-493-2019.

Goovaerts, Pierre. 1997. *Geostatistics for Natural Resources Evaluation*. Oxford University Press. https://doi.org/10.1093/oso/9780195115383.001.0001.

Gurrieri, J. T., et G. Furniss. 2004. « Estimation of groundwater exchange in alpine lakes using non-steady mass-balance methods ». *Journal of Hydrology* 297 (1): 187-208. https://doi.org/10.1016/j.jhydrol.2004.04.021.

Hall, Dorothy, et George Riggs. 2016. « MODIS/Terra Snow Cover Daily L3 Global 500m SIN Grid, Version 6 ». NASA National Snow and Ice Data Center Distributed Active Archive Center. https://doi.org/10.5067/MODIS/MOD10A1.006.

Hurley, J. P., D. E. Armstrong, G. J. Kenoyer, et C. J. Bowser. 1985. « Ground Water as a Silica Source for Diatom Production in a Precipitation-Dominated Lake ». *Science (New York, N.Y.)* 227 (4694): 1576-78. https://doi.org/10.1126/science.227.4694.1576.

Jordan, Rachel E. 1999. « Heat budget of snow-covered sea ice at North Pole 4 - Jordan - 1999 - Journal of Geophysical Research: Oceans - Wiley Online Library ». https://agupubs.onlinelibrary.wiley.com/doi/10.1029/1999JC900011.

Kirchner, P. B., R. C. Bales, N. P. Molotch, J. Flanagan, et Q. Guo. 2014. « LiDAR Measurement of Seasonal Snow Accumulation along an Elevation Gradient in the Southern Sierra Nevada, California ». *Hydrology and Earth System Sciences* 18 (10): 4261-75. https://doi.org/10.5194/hess-18-4261-2014.

Kongoli, Cezar, et Thomas M. Smith. 2023. « Modeling and Estimation of Snow Depth Spatial Correlation Structure from Observations over North America ». *Frontiers in Earth Science* 11 (janvier). https://doi.org/10.3389/feart.2023.1035339.

Lee, Won Young, Hyeon-Ju Gim, et Seon Ki Park. 2024. « Parameterizations of Snow Cover, Snow Albedo and Snow Density in Land Surface Models: A Comparative Review ». *Asia-Pacific Journal of Atmospheric Sciences* 60 (2): 185-210. https://doi.org/10.1007/s13143-023-00344-2.

Niang, Mohamed, Monique Bernier, Eric Van Bochove, et Yves Durand. 2006. « Précision de l'estimation de l'équivalent en eau de la neige obtenue avec lasonde SNOWPOWER au Québec (Canada) ». *La Houille Blanche* 92 (2): 128-33. https://doi.org/10.1051/lhb:200602017.

OFEV. 2024. « Bassins versants topographiques des eaux suisses : bassins versants partiels de 2 km^2 - Bassins versants topographiques des eaux suisses : bassins versants partiels de 2 km^2 - opendata.swiss ». https://opendata.swiss/fr/dataset/topographische-einzugsgebiete-der-schweizer-gewasser-teileinzugsgebiete-2km2/resource/0b9e39b0-40bf-4ce8-bb22-3c433f7b5fbe.

« Open Data - MétéoSuisse ». s. d. Consulté le 29 juillet 2025. https://www.meteosuisse.admin.ch/services-et-publications/service/open-data.html.

Ordóñez, Cesar Fernando. 2022. « Oxic Methane Production Dynamics in Lakes ». Université de Genève.

Parriaux, Adrien. 1997. « Dimensionnement des zones de protection des eaux des sources du Poutet et du Tunnel ». Dropbox. https://www.dropbox.com/scl/fi/mt6n2gpq8dufy8kzmd0hu/Rapport-Geolep-Ollon-ZP-Sources-du-Poutet-et-du-Tunnel.pdf?dl=0&e=1&rlkey=zrza0y5cg7gth8cmci5t8b1rh.

Pomeroy, J.W., et E. Brun. 2001. *Physical Properties of Snow*. https://www.inscc.utah.edu/~campbell/snowdynamics/reading/Pomeroy.pdf.

Poussin, Charlotte, Pascal Peduzzi, et Gregory Giuliani. 2025. « Snow observation from space: An approach to improving snow cover detection using four decades of Landsat and Sentinel-2 imageries across Switzerland ». *Science of Remote Sensing* 11 (juin): 100182. https://doi.org/10.1016/j.srs.2024.100182.

Rabatel, Antoine, Etienne Berthier, Yves Arnaud, et al. 2017. « Télédétection satellitaire des surfaces enneigées et englacées ». *La Météorologie*, Observation satellitaire, n° 97 (mai): 78-85. https://doi.org/10.4267/2042/62170.

Rolland, Christian. 2003. *Spatial and Seasonal Variations of Air Temperature Lapse Rates in Alpine Regions*. Journal of Climate. avril 1. https://journals.ametsoc.org/view/journals/clim/16/7/1520-0442_2003_016_1032_sasvoa_2.0.co_2.xml.

« SAR Wet Snow 2016-Present (Raster 60 m), Europe, Daily ». s. d. Consulté le 24 juin 2025. https://land.copernicus.eu/en/products/snow/high-resolution-sar-wet-snow.

Swisstopo. 2004. « MNT25 ». https://www.swisstopo.admin.ch/fr/modele-altimetrique-mnt25.

Swisstopo. 2024. « Geological atlas of switzerland ». https://www.swisstopo.admin.ch/fr/atlas-geologique-de-la-suisse-1-25000.

Wang, Keli, Jia Sun, Guodong Cheng, et Hao Jiang. 2011. « Effect of Altitude and Latitude on Surface Air Temperature across the Qinghai-Tibet Plateau ». *Journal of Mountain Science* 8 (6): 808-16. https://doi.org/10.1007/s11629-011-1090-2.

« Wet/Dry Snow 2016-Present (Raster 60 m), Europe, Daily ». s. d. Consulté le 24 juin 2025. https://land.copernicus.eu/en/products/snow/high-resolution-wet-dry-snow.

Yu, Kegen. 2021. « Snow Depth and Snow Water Equivalent Estimation ». In *Theory and Practice of GNSS Reflectometry*, édité par Kegen Yu. Springer. https://doi.org/10.1007/978-981-16-0411-9_8.